minerals

Article

Influences of Water Content on Acousto-Mechanical Properties and Failure Behaviors of Triaxially Compressed Shale

Sui Zhang [1,2], Fuming Cai [3], Yangbing Cao [3,*] and Qiang Yan [3]

[1] Engineering Technology Innovation Center of Mineral Resources Explorations in Bedrock Zones, Ministry of Natural Resources, Guiyang 550081, China; zhangsui85697503@163.com
[2] 103 Geological Brigade of the Bureau, Geology and Mineral Exploration and Development in Guizhou Province, Tongren 554300, China
[3] Zijin School of Geology and Mining, Fuzhou University, Fuzhou 350108, China; cai_fuming@163.com (F.C.); yanqiang290161@163.com (Q.Y.)
* Correspondence: ybcao@fzu.edu.cn

Abstract: Due to the extreme water sensitivity of shale, the excavation of shale underground engineering is prone to major disaster accidents such as roof falls and collapses. However, current investigations have failed to fully explain the mechanisms by which water content affects shale damage behaviors. In this study, the acousto-mechanical properties and failure behaviors of laminated shale under different confining pressures σ_3 are investigated with the aid of AE monitoring for three different water content states. The results show that the shale strength decreases with the increase of the water content, but it increases as the confining pressure σ_3 increases. For the shale, the change in the wetting angle and the distance between the centroids of the two adjacent particles inside the bedding plane is more prominent than the surrounding shale matrix, and the swelling pressure is generated among the clay minerals, which are the two main mechanisms for the bedding-participating failure and the shale softening after immersion. Moreover, with the increase of the water content and σ_3, the damage mode of shale specimens gradually changes from tension damage to shear damage. Controlled by bedding, shale failure shows significant suddenness without clear acoustical precursors. This study provides experimental and theoretical bases for the stability analysis of shale underground engineering.

Keywords: water content; acoustic emission; failure characteristics; shale; triaxial compression experiment

check for updates

Citation: Zhang, S.; Cai, F.; Cao, Y.; Yan, Q. Influences of Water Content on Acousto-Mechanical Properties and Failure Behaviors of Triaxially Compressed Shale. *Minerals* **2023**, *13*, 1087. https://doi.org/10.3390/min13081087

Academic Editor: Gianvito Scaringi

Received: 24 June 2023
Revised: 7 August 2023
Accepted: 11 August 2023
Published: 15 August 2023

1. Introduction

The development of deep underground engineering often leads to major disasters, such as roof caving and collapse, which pose a serious threat to underground workers. Shale has the characteristics of bedding and easy degradation in water, which can easily cause engineering problems (Martin et al. [1]). Thus, studies on the influence of water content on the acousto-mechanical properties and failure behaviors of shale during experiments have important theoretical and practical significance for the stability evaluation of underground engineering.

The mechanical properties of rock have an important influence on the stability of the surrounding rock. Water content is an important factor affecting the physical and mechanical properties of rocks (Wong et al. [2], Li and Wang [3]). To study the influence of water content on the mechanical properties of sandstone, some scholars (Roy et al. [4], Li et al. [5], Luo et al. [6], Zhang et al. [7], Wang et al. [8]) carried out uniaxial and triaxial mechanical tests. The results showed that the strength and elastic modulus of sandstone show a decreasing trend with the increase of water content, and the water in sandstone has a softening effect on cementing materials and mineral particles. The higher the water content, the more obvious the softening effect. The previous works had carried out some research on the effect of water on the mechanical properties of granite by conducting indoor mechanical tests (Man et al. [9], Zhang et al. [10], Zhou et al. [11]). The experimental results showed that the peak strength and elastic modulus of saturated granite are lower than those of dry granite. The softening effect of water content on the strength of slate was further investigated via indoor experiments (Zhang et al. [12], Lv [13], Chen et al. [14]), and their results showed that the water content can weaken the mechanical properties of slate. Cai et al. [15] found that the calcite cementation between particles gradually dissolved and the density and width of intergranular cracks increased after the dry–wet cycle, which may be the reason for the deterioration of the mechanical properties of sandstone. Chen et al. [16] found that the hydration, hydrolysis and dissolution processes co-occur inside the rock, but the hydration expansion effect was greater than the hydrolysis and dissolution effects. Li et al. [17] found that the parameters of rocks, such as peak compressive strength, peak axial strain, cohesion and internal friction angle, decreased nonlinearly with the increase of pore pressure in the experimental results and theoretical research. In addition, Du et al. [18] used acoustic emission (AE) technology to analyze the AE characteristics of granite, marble and sandstone, for a better understanding of the essential differences of failure modes among them. Zhang and Zhou [19,20] used an AE technique to conduct uniaxial compression tests on sandstone and granite with prefabricated cracks, and they found that acoustic quiescence of flawed sandstone and granite had a mechanistic link and quantitative correlation with the stress drop.

Shale is a typical sedimentary rock and its bedding structure affects the final failure mode. Many researchers (Niandou et al. [21], Kuila et al. [22], Xu et al. [23], Yang et al. [24]) have studied the influence of bedding angle on the shale failure modes and mechanical properties using uniaxial and triaxial compression tests. The results showed that the compressive strength of shale follows a "U-shaped" path, showing obvious anisotropy. The anisotropy of shale fracture mode is closely related to the bedding dip angle and confining pressure. Water content is an important factor affecting the mechanical properties and failure modes of shale. Some researchers (AL-Bazali [25], Sone et al. [26], Rybacki et al. [27], Lyu et al. [28]) have explored the influence mechanisms of water content on the strength and deformation of shale. The results showed that the strength and elastic modulus of shale decrease with the increase of water content, and that the presence of water increases the deformation of shale. In addition, Ban et al. [29] studied the correlation between the meso-scale damage mechanism and the macro-scale cracking behavior of shale with prefabricated cracks through the moment tensor inversion of AE signals.

The current contributions in the study field of the mechanical properties and failure characteristics of rocks are of great significance to the stability evaluation of underground engineering. However, the influence mechanism of different water contents and confining pressures of bedding shale remains unclear, and the engineering phenomenon cannot be fully explained. In this study, uniaxial and triaxial compression tests combined with AE technology were carried out on shale specimens with three moisture states (natural, immersion in water for 12 h and saturation) to comprehensively study the effects of water content and confining pressure on the shale's acousto-mechanical properties. The innovation of this study is manifested in the following two aspects: (1) The acoustic emission characteristics of the failure process of water-bearing shale were studied by combining acoustic emission technology and time-reversed Omori's law. (2) The microscopic mechanism of water softening failure of shale is summarized and revealed. The experimental results can provide experimental and theoretical bases for the stability analysis of deep shale underground engineering.

2. Experiments

A long series of standard shale specimens (uniaxial compression strength of ~141.64 MPa) were prepared for the present study, according to the Standard for Test Methods for Engineering Rock (GB50266-2013). The mineralogical composition of shale was determined by an XRD experiment using a D8 ADVANCE DaVinci X-Ray Automatic Diffractometer from Bruker, Germany. The test results are shown in Figure 1. The shale minerals were mainly defined as quartz, muscovite and albite with a total content of approximately 91.1%; the clay mineral was chlorite with a total content of approximately 5.4%. The P-wave velocities of the shale specimens at different experiments were nearly consistent with each other, as shown in Table 1, indicating the high homogeneity of the tested shale material.

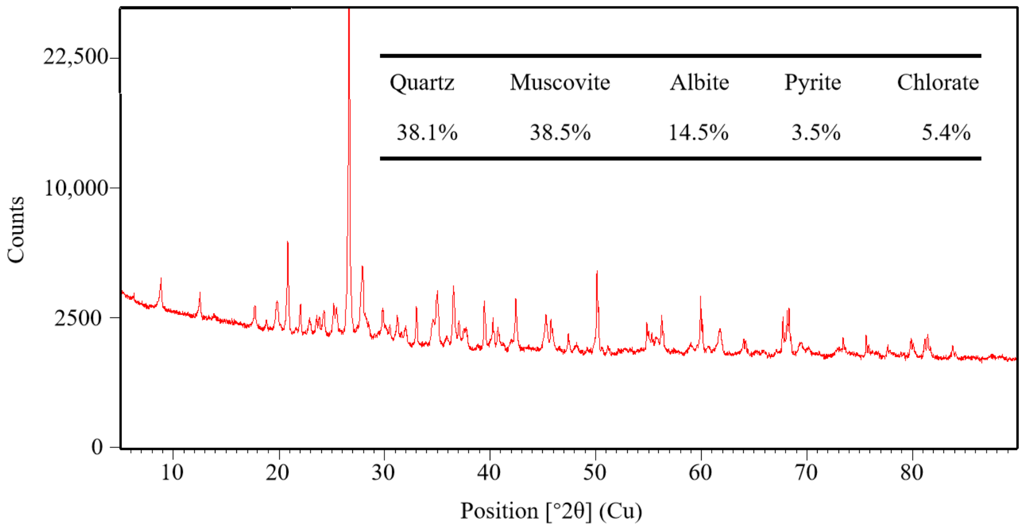

Figure 1. XRD testing results of shale.

Table 1. Basic parameters of shale.

Specimen	Diameter /mm	Height /mm	Confining Pressure /MPa	Water Content/%	Average Water Content/%	P-Wave Velocity/m/s
Natural	50.2	100.1	0	0.47	0.46	3792
	50.2	100.2	10	0.44		3795
	50.4	100.3	20	0.46		3980
	50.2	100.9	30	0.48		3793
Immersion for 12 h	50.2	100.1	0	0.85	0.88	3910
	50.2	100	10	0.86		3906
	50.2	100.1	20	0.88		3880
	50.2	100.1	30	0.91		3821
Saturation	50.2	100.2	0	1.55	1.55	3795
	50.3	100.2	10	1.52		3883
	50.2	100.1	20	1.54		3850
	50.2	100.5	30	1.58		3957

Note: P-wave velocity of the shale with the 90° bedding angle is presented.

To understand the effects of water content and confining pressure on the shale's acousto-mechanical properties and failure behaviors, four kinds of confining pressure σ_3 (0, 10, 20, 30 MPa) and three kinds of different water contents ω (natural, immersion for 12 h and saturation) are designed. Figure 2 shows some of the shale specimens and the bedding dip diagram. Table 1 shows the details of the experimental set-up. The specimens immersed for 12 h were obtained with the free immersion method, and the saturated specimens were obtained with the vacuum pumping method. When the vacuum pumping method is used to saturate the specimen, the water surface in the saturated container should be higher than that of the specimen, and the reading on the vacuum gauge should be the local atmospheric pressure value. Pump until no bubbles escape, but the pumping time should not be less than 4 h. After vacuum pumping, the specimen should be placed in the original container and left at atmospheric pressure for 4 h.

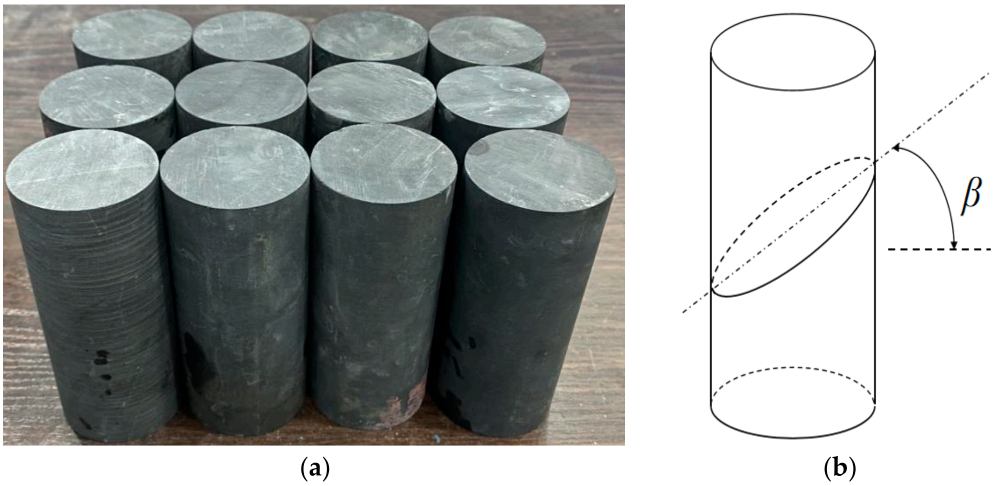

Figure 2. Some of the shale specimens and bedding dip diagram. (**a**) The specimens of shale; (**b**) schematic diagram of shale bedding angle. β is the bedding dip angle with respect to the horizontal plane.

The uniaxial and triaxial compression experiments were carried out by a TAJW-2000 triaxial testing system, which has a maximum axial load of 2000 kN (Figure 3). The experiments were conducted at a constant displacement control loading rate of 0.1 mm/min. During the experiments, the AE signals were detected by four RS-2A sensors in a Beijing Soft Island DS5 AE monitoring system (Figure 3). The pre-amplifiers were set as 40 dB, the signal threshold was 45 dB and the sampling rate was 5 MHz. To ensure that the sensor effectively received the AE signals, Vaseline was used to ensure the good coupling of the surface of the specimen and sensors.

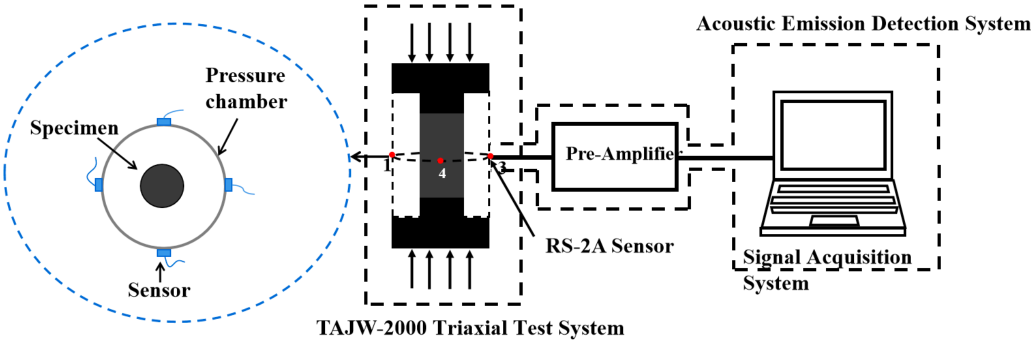

Figure 3. Experimental equipment.

As shown in Figure 4, the sketch shows the study of the shale compression failure mode to better visualize the failure state of the specimens throughout the rest of this paper.

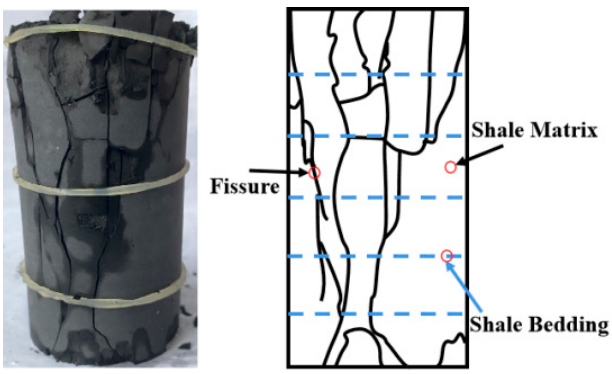

Figure 4. Sketch of shale specimen failure.

3. Experimental Results

3.1. Stress–Strain Responses

The stress–strain curves for shale specimens with different water contents are shown in Figure 5. The stress–strain curves for all specimens under compression show a quite consistent trend, whatever the confining pressure and the water content, featuring a large stress drop at the end of tests. At the beginning of the tests, the stress–strain curve is concave and the specimen deformation is dominated by the pore compaction, so this stage is termed the crack closure stage. As the loading proceeds, the curve shows a linear feature, and the specimen deformation is dominated by the elastic deformation stage. After that, the crack initiation in shale is triggered and progressively transitions into the unstable cracking stage. Driven by the large stress at the peak point, the curve drops rapidly, which is typical of a brittle nature. It can be observed from Figure 4 that as the water content increases, the strain value corresponding to the crack closure stage increases somewhat, and the curve growth rate of the elastic deformation stage becomes slower, followed by the peak strain at the onset of the peak stress generally increasing.

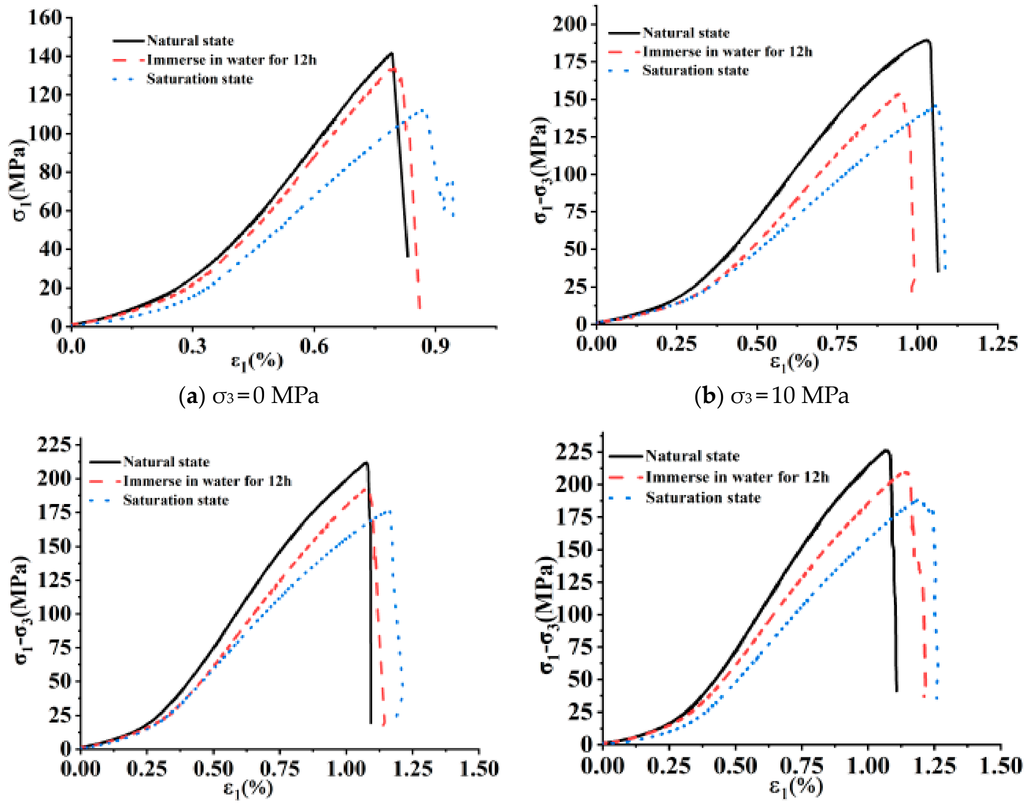

(**a**) σ_3 = 0 MPa (**b**) σ_3 = 10 MPa

(**c**) σ_3 = 20 MPa (**d**) σ_3 = 30 MPa

Figure 5. Stress–strain curve of shale with different ω. σ_1-σ_3 is the difference stress defined as the difference between the axial stress σ_1 and the confining pressure σ_3.

The basic mechanical parameters of shale are shown in Table 2. Under the same ω, the peak strength and peak strain of the specimens increase with the increase of the confining pressure σ_3. When σ_3 increases from 0 MPa to 30 MPa, the peak strength of the specimens in the natural state increases by 81.39% from 141.64 MPa to 256.92 MPa, and the corresponding peak strain increases from 0.791% to 1.071%. The peak strength of the specimens immersed for 12 h increases by 76.85% from 133.85 MPa to 236.72 MPa, and the corresponding peak strain increases from 0.799% to 1.147%. The peak strength of saturation specimens increases by 98.63% from 111.88 MPa to 222.23 MPa, and the corresponding peak strain increases from 1.060% to 1.2%.

Table 2. Experimental data of basic mechanical parameters of shale specimens.

Specimen State	Confining Pressure /MPa	Peak Strength /MPa	Peak Strain /%	Elastic Modulus /GPa
Natural	0	141.64	0.791	25.924
	10	199.57	1.034	28.382
	20	231.47	1.059	29.808
	30	256.92	1.071	30.406
Immersion for 12 h	0	133.85	0.799	23.391
	10	163.64	0.945	24.035
	20	210.81	1.069	24.955
	30	236.72	1.147	26.45
Saturation	0	111.88	0.864	18.354
	10	156.44	1.060	19.182
	20	196.01	1.159	21.551
	30	222.23	1.200	22.839

Moreover, at the same σ_3, the peak strength of the specimens decreases linearly with the increase of ω. Under 0 MPa confining pressure, the peak strength decreases from 141.64 MPa to 111.88 MPa with a decrement of 20.88%. Under 10 MPa confining pressure, the peak strength decreases by 21.61% from 199.57 MPa to 156.44 MPa. Under 20 MPa confining pressure, the peak strength decreases by 15.32% from 231.47 MPa to 196.01 MPa. Under 30 MPa confining pressure, the peak strength decreases by 13.50% from 256.92 MPa to 222.23 MPa. Under 10 MPa confining pressure, the decrease is greatest and the decrease value is also the greatest at 43.13 MPa.

Figure 6 shows the relationships between the shale strength (and also elastic modulus) and ω, along with the shale strength (and also elastic modulus) and confining pressure, in a three-dimensional parametric space. To clearly observe the dependency of shale properties on ω and confining pressure, the fitting surface is delineated in the three-dimensional parametric space. It can be found from Figure 6 that the shale strength and elastic modulus have a linear negative relationship with ω and a nonlinear relationship with the confining pressure.

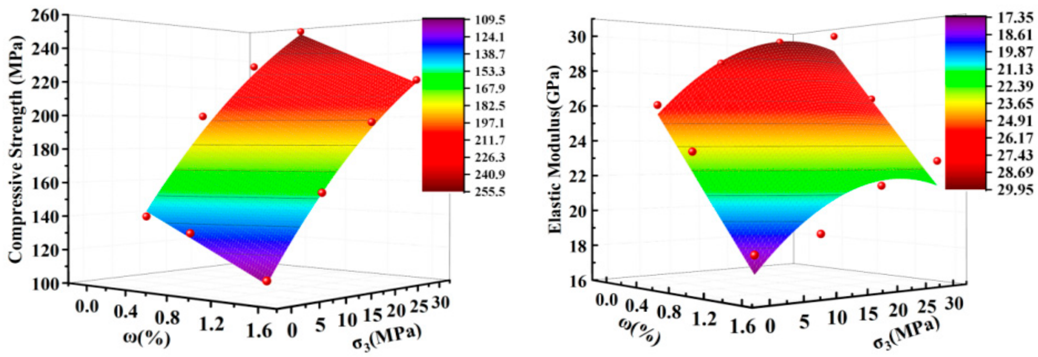

(**a**) Peak strength fitting surface (**b**) Elastic Modulus fitting surface

Figure 6. The relationships (**a**) between the shale strength and the involved parameters (ω and σ_3), along with (**b**) between the elastic modulus and the involved parameters.

3.2. Acousto-Mechanical Characteristics and Failure Modes

The relationships between axial stress and AE counts in the run-up to final failure of shale with different ω at different σ_3 conditions are shown in Figures 7–10. The AE characteristics of the whole loading process under different testing conditions have similar patterns. Dense AE activities are detected only when the external stress closely approaches the shale strength. More concretely, the cumulative AE count curve rises rapidly in the approach to the shale strength, and the ascending rate of cumulative AE count close to ultimate failure is much larger than that at the previous loading stages. Due to the dense shale microstructure, the AE activities during the crack closure stage and the elastic deformation stage are relatively sparse. These results indicate that the microcracks extend and penetrate in a very short time to generate the energetic failure, demonstrating that the shale is a typical brittle material.

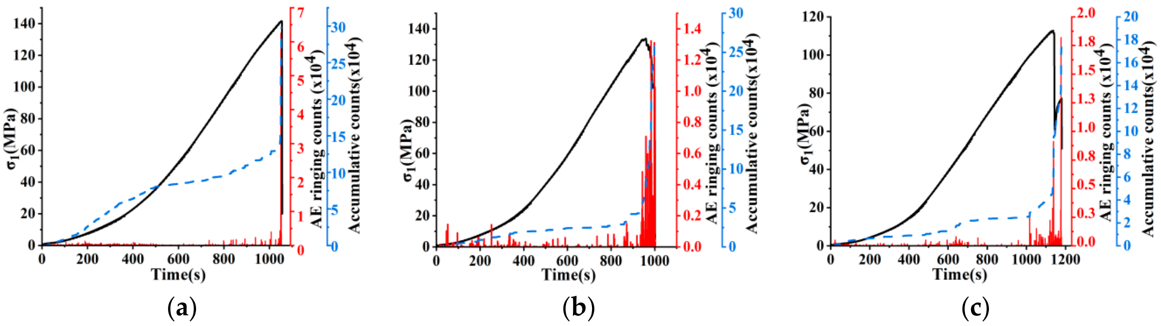

Figure 7. The relationship between AE counts and stress under σ_3 = 0 MPa with different moisture states. (**a**) Natural state; (**b**) immersion for 12 h; (**c**) saturation state.

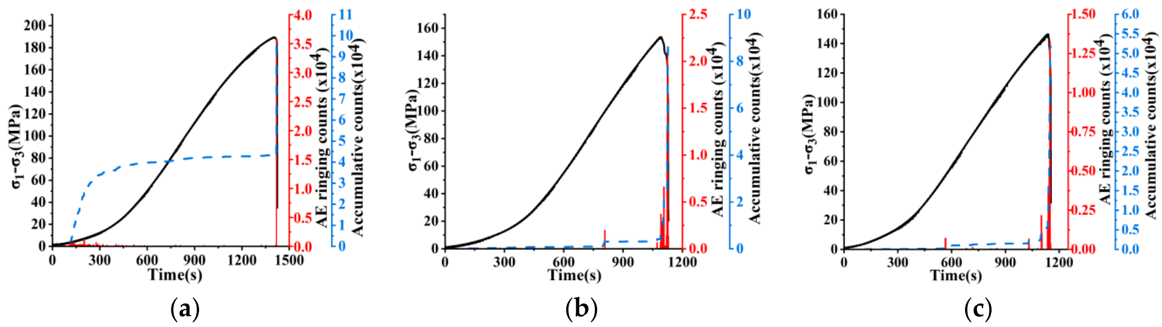

Figure 8. The relationship between AE counts and stress under σ_3 = 10 MPa with different moisture states. (**a**) Natural state; (**b**) immersion for 12 h; (**c**) saturation state.

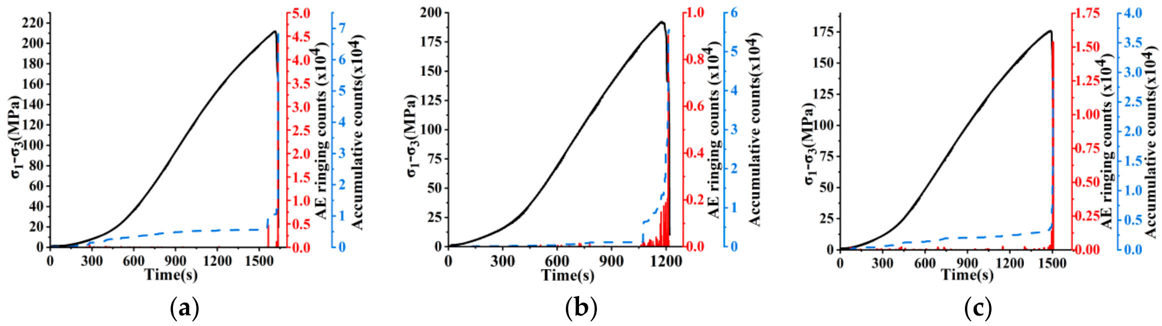

Figure 9. The relationship between AE counts and stress under σ_3 = 20 MPa with different moisture states. (**a**) Natural state, (**b**) immersion for 12 h; (**c**) saturation state.

The relationships between compressive strength and maximum cumulative AE count of shale and ω are shown in Figure 11, respectively. In general, with the increase of ω, the compressive strength and the maximum cumulative AE counts of shale gradually decrease, which is related to the degree of hydration of shale under different water content conditions. The XRD mineral composition analysis results in Figure 1 provide the interpretation for the above statement.

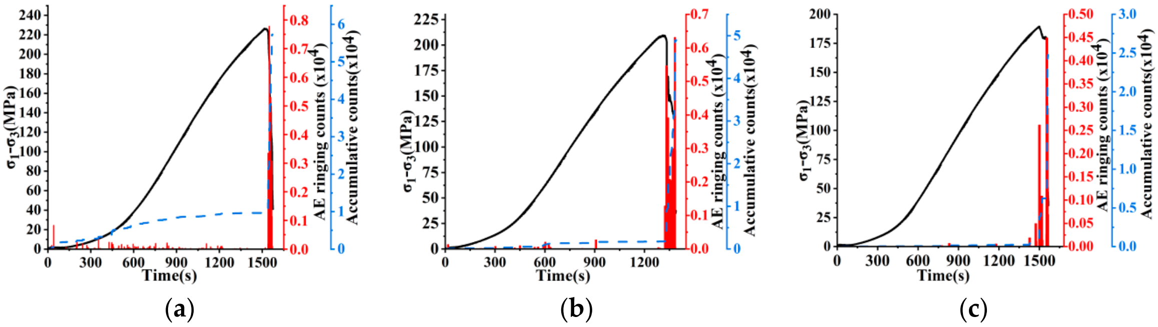

Figure 10. The relationship between AE counts and stress under σ_3 = 30 MPa with different moisture states. (**a**) Natural state, (**b**) immersion for 12 h; (**c**) saturation state.

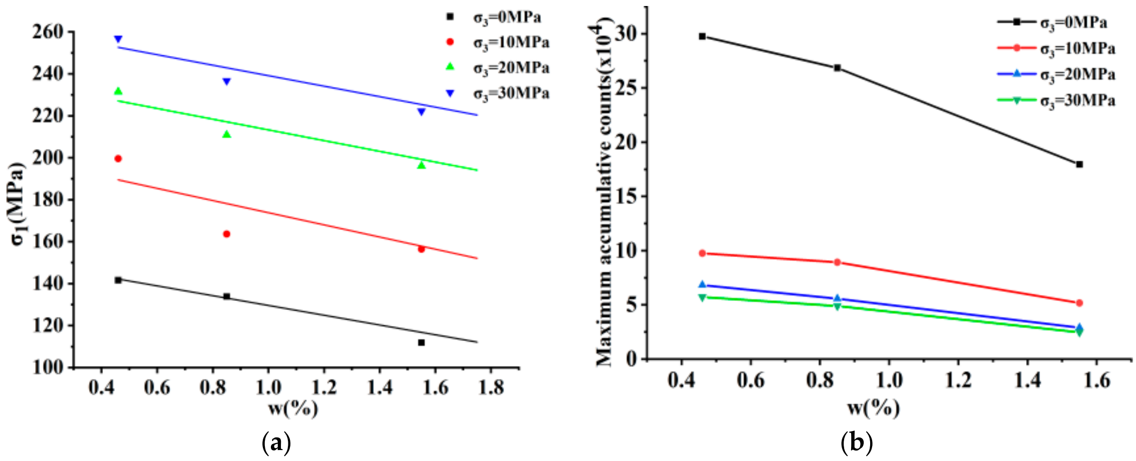

Figure 11. The relationships (**a**) between the shale strength σ_1 and water content ω, and (**b**) between the max AE accumulative counts and water content ω.

The failure behaviors of shale specimens with different ω under different σ_3 conditions are shown in Figures 12–15. The main failure plane of the natural state specimen under uniaxial condition is a tensile-dominated failure plane which penetrates the shale bedding. Under the condition of triaxial compression with σ_3 = 10 MPa, the failure plane of the specimen is the tensile failure shown by the formation of the penetrating cracks sub-orthogonal to the bedding plane. In terms of σ_3 = 20 MPa, the failure type is mainly the mixed tensile-shear failure, which is composed of a tensile failure plane sub-orthogonal to the bedding plane and a shear failure plane with a large angle with respect to the σ_1-direction. When σ_3 = 30 MPa, the failure type is an X-shaped conjugate shear failure. As the σ_3 increases, the failure mode of the natural state specimen gradually changes from tensile failure to shear failure.

Under the condition of uniaxial compression, with the increase of ω, the number of shear cracks through the bedding and transverse cracks along the bedding plane increases, and the failure mode changes from tensile failure to mixed tensile–shear failure. Under the natural state, no transverse cracks along the bedding plane are observed. Under 12 h immersion state, a transverse crack along the bedding plane is observed at the midst of the specimen. Under saturation state, the specimen produces multiple transverse cracks with different lengths, and these transverse cracks of different lengths intersect with the tensile cracks that extend towards σ_1. Under the condition of triaxial compression, as ω increases, the failure modes are more significantly affected by the shear cracks, and the specimens after failure is more broken. Taking σ_3 = 10 MPa as an example, no transverse cracks along the bedding plane are observed under the natural state. Under 12 h immersion state, a small number of transverse cracks along the bedding plane can be clearly observed. Under saturation state, the specimen produces multiple transverse cracks of different lengths and they also intersect with the tensile cracks. These transverse cracks along the bedding plane significantly increase the damage and fragment degree of the specimen, indicating that the participation of the bedding in the failure process is significantly enhanced.

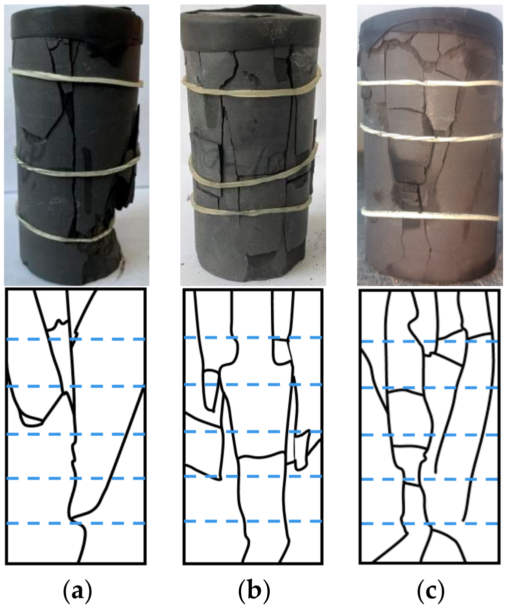

Figure 12. Failure morphology of specimens under σ_3 = 0 MPa with different ω. (**a**) Natural state, (**b**) immersion for 12 h, (**c**) saturation state.

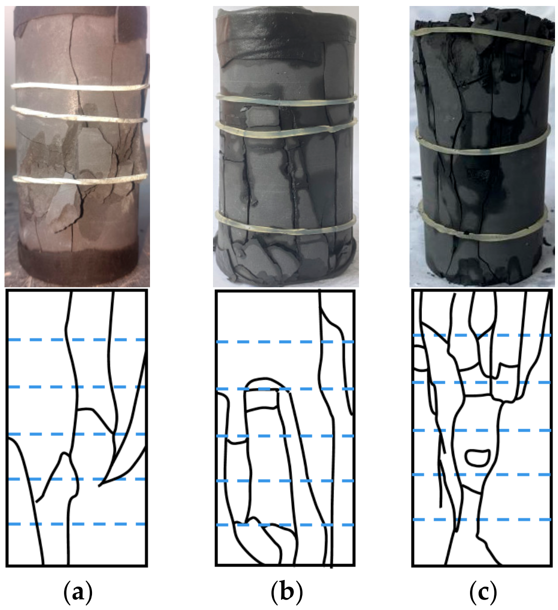

Figure 13. Failure morphology of specimens under σ_3 = 10 MPa with different ω. (**a**) Natural state, (**b**) immersion for 12 h, (**c**) saturation state.

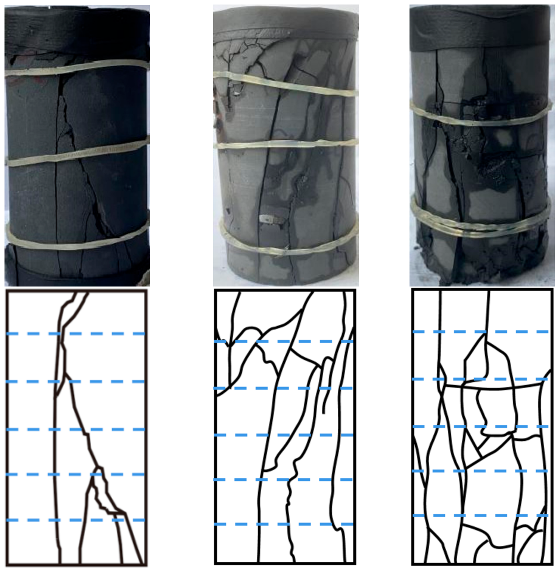

Figure 14. Failure morphology of specimens under σ_3 = 20 MPa with different ω. (**a**) Natural state, (**b**) immersion for 12 h, (**c**) saturation state.

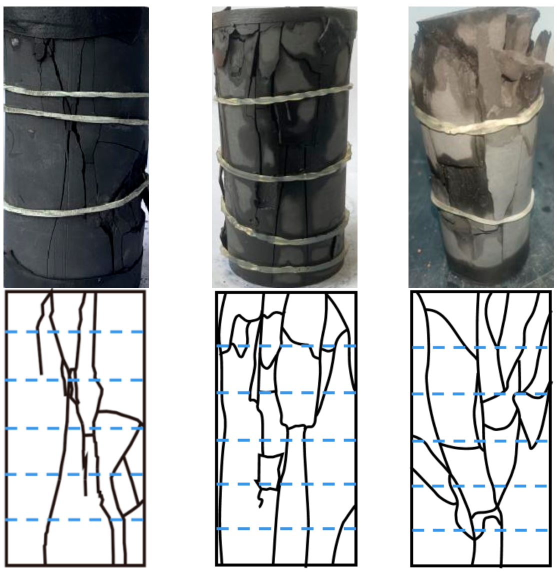

Figure 15. Failure morphology of specimens under σ_3 = 30 MPa with different ω. (**a**) Natural state, (**b**) immersion for 12 h, (**c**) saturation state.

4. Discussions

4.1. Water Content Influencing Mechanism

The deterioration mechanisms of water on rock mainly include chemical effects, capillary pressure and adsorption (Yang et al. [30]). However, considering that chemical action is a long process far beyond the shale immersion time in the laboratory, the influence of the chemical action between water and mineral particles on the shale is not considered in this study.

Figure 16 shows the schematic change of the force between shale mineral particles in water. In natural state, not all pores in shale have water phase. With the increase of soaking time, the ω of the specimen increases gradually, and water fills the pores until it is saturated. The calculation formulae of cohesion F and capillary pressure P_c between particles are expressed as follows (Yang et al. [30]):

$$F = F_g + P_c + F_1 + F_2 + \sigma_s + P_w \quad (1)$$

$$P_c = \frac{\cos(\phi + \theta)}{\cos \phi} \frac{\sigma_s}{R} \quad (2)$$

where F_g is the interaction force between particles, F_1, F_2 represent the strong force and weak force between particles and water, respectively, σ_s is the surface tension of particles, P_w is the pressure of water, φ is the angle between the axial connection of particles and the tangential radius direction of the particle–air contact point, θ is the wetting angle and R is the distance between the centroids of the two adjacent particles.

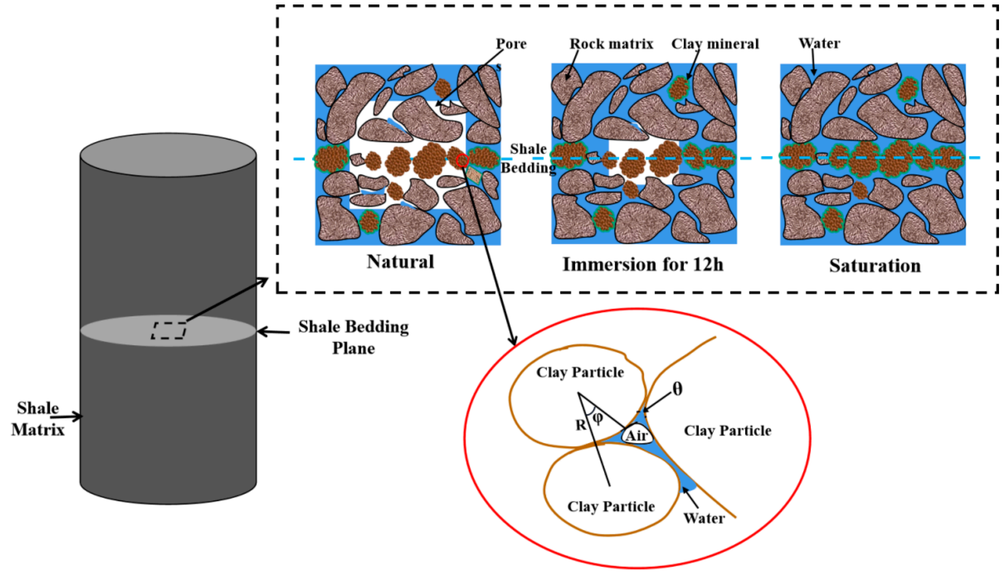

Figure 16. A schematic diagram of the change of the interaction force between mineral particles in shale under the water environment.

When the shale specimen is immersed in water, the clay particles absorb water and thus expand, resulting in the increase of the distance R between the centroids of the two adjacent particles, as illustrated in Figure 16. According to Equations (1) and (2), it can be noticed that the interaction force between the particles decreases when R increases. At the same time, the wetting angle θ decreases with the increase of water absorption, resulting in the gradual decrease of capillary pressure and surface tension, which reduces the cohesion between particles. For the shale, the bedding plane serves as a weak link relative to the surrounding shale matrix. Thereby, the change in R and θ inside the bedding plane is more prominent than the surrounding shale matrix. This is one mechanism for the shale softening and the resulting strength reduction after immersion. Another mechanism lies in the generation of the swelling pressure among the clay minerals due to the water absorption. The clay minerals within the shale are small and hydrophilic, and the clay minerals such as chlorite near the bedding plane are apt to swell to generate swelling pressure when water enters the pores and fissures of shale. As ω increases, the adsorbed water film of fine rock particles thickens, and some cements are therefore softened and possibly dissolved, resulting in the collapse, disintegration and volume expansion of the lamellar structure (Zhu et al. [31]). Interestingly, such mechanisms can be well supported by the failure patterns of shale that is solely under immersion, as shown in Figure 16. The laminated shale in this study disintegrates along the bedding plane during water immersion (without the loading) in Figure 17, reflected by the fact that the whole shale is broken into 2–3 sub-blocks during the immersion.

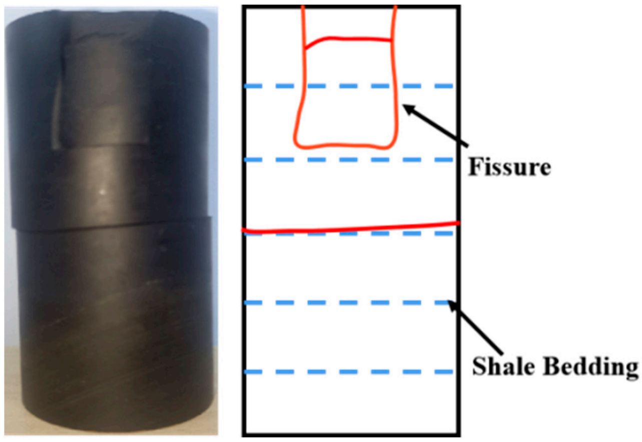

Figure 17. Shale collapses after immersing in water.

Combined with the analysis of Figures 16 and 17, it can be seen that under the combined action of expansion stress and softening or dissolution of colloid, shale is prone to crack along the bedding surface during the loading process of the specimen with the increase of ω.

4.2. Confining Pressure-Influencing Mechanism

The relationships between the triaxial compressive strength of the shale specimens and σ_3 are shown in Figure 18, as well as the relationships between the maximum cumulative AE counts and σ_3. In general, the compressive strength of the shale specimens increases and the maximum cumulative AE counts gradually decrease with the increase of σ_3. Under the condition of triaxial compression, σ_3 constrains the lateral deformation of the specimen and promotes the increase of the compressive strength of the specimen. Some of the original structural planes or micro-cracks of the specimens may be closed, which reduces the AE events and the AE counts in the compaction stage. This is one interpretation of the reduction of the AE activities. In addition, due to the constraint of the lateral deformation of the specimen by σ_3, the relative moving of internal grains is mechanically inhibited, such that the stress wave is not generated.

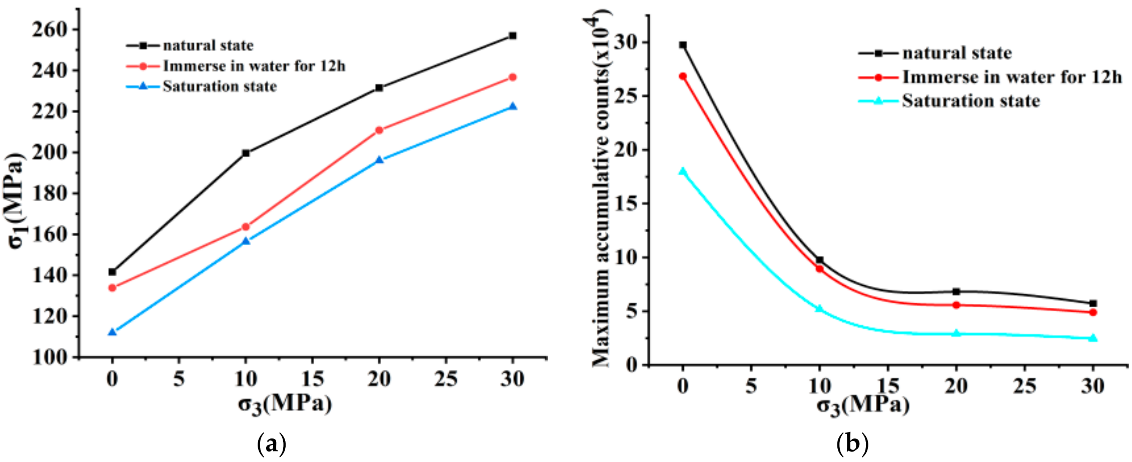

Figure 18. The relationships (**a**) between the shale strength σ_1 and confining pressure σ_3, along with (**b**) between the max AE accumulative counts and confining pressure σ_3.

AE amplitude represents the maximum amplitude of a single AE event, which can be used to characterize the strength of AE events. The AE amplitude distribution in terms of the magnitude under different σ_3 is shown in Figure 19. The AE amplitude is mainly distributed within 45–65 dB, accounting for more than 90%. With the increase of σ_3, the proportion of small AE events gradually increases, while the number of high-amplitude AE events (>65 dB) gradually decreases. This is mainly because the lateral constraint of the rock specimen is greater and the initiation of internal cracks is restricted with the increase of σ_3. The stored energy in the shale is mainly consumed by shear friction, thus reducing the proportion of the high-amplitude events. Under the condition of σ_3 = 10 MPa, the proportion of amplitude higher than 65 dB in saturated shale under σ_3 of 10 MPa increases instead, because the pore pressure of the specimen in saturated state promotes the macroscopic crack initiation beyond the effects of σ_3 confinement.

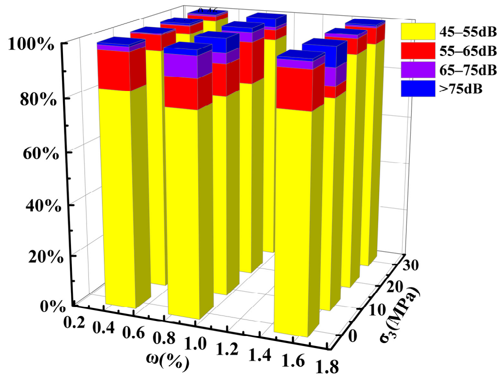

Figure 19. AE amplitude distribution of shale under different σ_3.

4.3. AE-Rate Process Analysis

In data processing, only the AE sensor that collects the most AE signals is targeted for the quantitative rate-process analysis. To be specific, the inter-event time interval (IET) function $F(\tau)$ is introduced to describe the characteristics of AE event rate related to rupture. Firstly, the IET mean of N consecutive AE events is calculated as follows (Zhang et al. [32]):

$$\tau_i = \frac{t_i - t_{i-N}}{N}(i = N + 1, N + 2, \ldots) \tag{3}$$

where t_i denotes the instant when the ith AE event occurs, and t_{i-N} denotes the instant when the (i−N)th AE event occurs. The function $F(\tau)$ is defined as the reciprocal of IET, and the formula is as follows:

$$F(\tau_i) = {\tau_i}^{-1}(i = N + 1, N + 2, \ldots) \tag{4}$$

The N value is 100 in the calculation. The N value is generally much smaller than the total number of AE events recorded in the test. For the traditional analysis method of characterizing AE activity in seconds, the calculation step is generally defaulted to 1 s; that is, each second can only correspond to one information point. For the theory of the acoustic emissivity process, the calculation step is actually the AE event itself. Taking function $F(\tau_i)$ and function $F(\tau_{i+1})$ as an example, the former reflects the influence of the occurrence of the current event on the AE event rate, while the latter reflects the influence of the occurrence of the next event on the AE event rate (Triantis and Kourkoulis [33]). Therefore, the theory of the AE rate process can analyze the AE activity produced by the damage and fracture process of rock specimens more accurately.

Taking σ_3 = 0 MPa and σ_3 = 30 MPa as examples for analysis, the results are shown in Figures 20 and 21. When the stress drops from the peak, the AE increases dramatically, demonstrating that the crack propagation can be monitored in real time via AE. However, whatever the ω and the σ_3, a clear acoustical precursor in the approach to ultimate failure of shale is not registered in Figures 20 and 21, so that the prediction of shale failure is difficult to achieve using a deterministic physical law (such as time-reversed Omori's law) (Zhang et al. [32]). It should be mentioned that the precursory laws in the approach to rock failure depend on the rock types, specifically the rock microstructures. Current shale data present obvious differences from uniaxial compression experiments on sandstone and granite (Zhang and Zhou [19,20]) and the conventional triaxial compression experiments of sandstone (Lennartz-Sassinek et al. [34]). Previous works (Lennartz-Sassinek et al. [34], Zhang and Zhou [19,20]) show a predictability of the failure time of sandstone and granite using their precursory AE time series, but this does not work in the current study. The underlying mechanism may lie in the fact that the deformation, damage and instability of shale are closely related to its internal bedding plane. Because of the low strength, the bedding plane serves as the weak link and controls the shale strength. That is to say, the stored energy in shale is dissipated mainly in the form of the bedding deformation and damage. When the strength of the bedding plane is in a subcritical state, the overall instability of the shale specimens is very imminent without apparent precursory features.

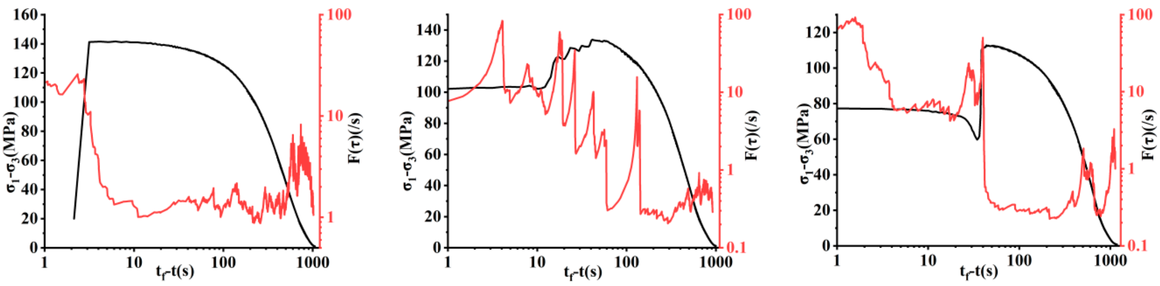

(a) (b) (c)

Figure 20. The relationship between differential stress, F(τ) and t_f-t under σ_3 = 0 MPa with different ω. (**a**) Natural state, (**b**) immersion for 12 h, (**c**) saturation state.

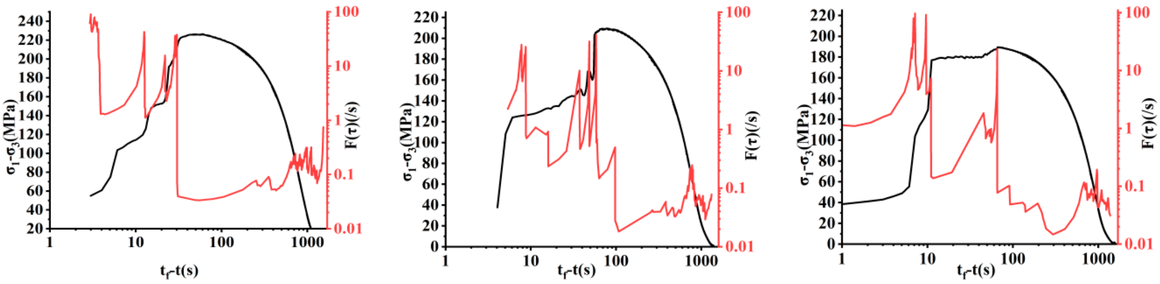

(a) (b) (c)

Figure 21. The relationship between differential stress, F(τ) and t_f-t under σ_3 = 30 MPa with different ω. (**a**) Natural state, (**b**) immersion for 12 h, (**c**) saturation state.

5. Conclusions

The influences of the water content on the acousto-mechanical properties and failure behaviors of shale were investigated under uniaxial and triaxial compression using AE monitoring techniques. The main conclusions can be drawn as follows:

(1) The strength of shale specimens decreases with the increase of the water content ω, but it increases as the confining pressure σ_3 increases. Generally, the peak strain increases with the increase of ω, except for the case of σ_3 = 10 MPa. The elastic modulus has a linear negative correlation with ω and a nonlinear positive correlation with σ_3.

(2) For the shale, the bedding plane serves as a weak link relative to the surrounding shale matrix. Thereby, the change in the wetting angle θ and the distance R between the centroids of the two adjacent particles inside the bedding plane is more prominent than the surrounding shale matrix. This is one mechanism for the shale softening and the resulting strength reduction after immersion. Another mechanism lies in the generation of the swelling pressure among the clay minerals due to the water absorption.

(3) The AE rate process analysis shows that the evolution of the precursor field for rock instability is closely related to the rock microstructure. In the case of shale, the strength

failure is often controlled by the laminae, and therefore shale failure shows significant abruptness without precursors.

This paper provides an experimental method for interpretations of the shale failure in response to the change in water content under triaxial compression. The conclusions apply at the scales investigated. To gain a better understanding of shale failure mechanisms, the upcoming investigations should focus on the different scales from the microscopic to macroscopic and establish their correlations. In particular, environmental scanning electron microscopy (ESEM) and nanoindentation investigation of the bedding plane characteristics of shale should be conducted experimentally in the near future.

Author Contributions: Conceptualization, S.Z.; methodology, F.C. and Q.Y.; software, F.C.; validation, S.Z.; formal analysis, F.C.; investigation, S.Z.; resources, S.Z.; data curation, F.C.; writing—original draft preparation, S.Z.; writing—review and editing, Y.C.; visualization, Q.Y.; supervision, Y.C.; project administration, S.Z.; funding acquisition, S.Z. All authors have read and agreed to the published version of the manuscript.

Funding: This research was funded by the Geological Research Project of Bureau of Geology and Mineral Exploration and Development Guizhou Province of China (Grant No. Qian Di Kuang Ke He [2020]-1) and by the Guizhou Province High Level Innovative Talent Project (Grant No. [2020]-6019).

Data Availability Statement: The data used to support the findings of this study are available from the corresponding author upon request.

Conflicts of Interest: The authors declare that there are no conflict of interest regarding the publication of this paper.

References

1. Martin, C.D.; Giger, S.; Lanyon, G.W. Behaviour of weak shales in underground environments. *Rock Mech. Rock Eng.* **2016**, *49*, 673–687. [CrossRef]
2. Wong, L.N.Y.; Maruvanchery, V.; Liu, G. Water effects on rock strength an-d stiffness degradation. *Acta Geotech.* **2016**, *11*, 713–737. [CrossRef]
3. Li, D.Y.; Wang, W.J. Quantitative analysis of the influence of saturation on rock strength reduction considering the distribution of water. *Geomech. Geophys. Geo-Energy Geo-Resour.* **2019**, *5*, 197–207. [CrossRef]
4. Roy, G.D.; Singh, T.N.; Kodikara, J.; Das, R. Effect of water saturation on the fracture and mechanical properties of sedimentary rocks. *Rock Mech. Rock Eng.* **2017**, *50*, 2585–2600. [CrossRef]
5. Li, D.Y.; Sun, Z.; Zhu, Q.Q.; Peng, K. Triaxial loading and unloading testson dry and saturated sandstone specimens. *Appl. Sci.* **2019**, *9*, 1689. [CrossRef]
6. Luo, Z.S.; Zhu, Z.X.; Bai, H.; Liu, D.X.; Sun, Q.C. Research on the influence of moisture condition on the mechanical properties and microstructure of sandstone. *Shock Vib.* **2021**, *2021*, 4850650. [CrossRef]
7. Zhang, C.; Wang, Y.; Ruan, H.; Ke, B.; Lin, H. The strain characteristics and corresponding model of rock materials under uniaxial cyclic load/unload compression and their deformation and fatigue damage analysis. *Arch. Appl. Mech.* **2021**, *91*, 2481–2496. [CrossRef]
8. Wang, F.; Wu, C.; Yao, Q.; Li, X.; Chen, S.; Li, Y.; Li, H.; Zhu, G. Instability mechanism and control method of surrounding rock of water-rich roadway roof. *Minerals* **2022**, *12*, 1587. [CrossRef]
9. Man, K.; Liu, X.L.; Song, Z.F.; Liu, Z.X.; Liu, R.L.; Wu, L.W.; Cao, Z.X. Dynamic compression characteristics and failure mechanism of water-saturated granite. *Water* **2022**, *14*, 216. [CrossRef]
10. Zhang, Y.H.; Ma, J.; Sun, D.Y.; Zhang, L.Y.; Chen, Y.C. AE characteristics of rockburst tendency for granite influenced by water under uniaxial loading. *Front. Earth Sci.* **2020**, *8*, 55. [CrossRef]
11. Zhou, H.W.; Wang, Z.H.; Ren, W.G.; Liu, Z.L.; Liu, J.F. Acoustic emission based mechanical behaviors of Beishan granite under conventional triaxial compression and hydromechanical coupling tests. *Int. J. Rock Mech. Min. Sci.* **2019**, *123*, 104125. [CrossRef]
12. Zheng, L.J.; Xie, H.; Xu, Z.X.; Deng, J.H.; Wang, D.; Zhang, G.Z.; Li, C.B.; Zhang, R.; Feng, G. A Comparison of Mechanical Properties and Failure Processes of Saturated and Unsaturated Slate from Sichuan-Tibet Plateau Area, China. *Lithosphere* **2022**, *2022*, 4503366. [CrossRef]
13. Lv, X.J. Exploring the deformation features and control techniques for surrounding rock of slate section tunnel. *Arab. J. Geosci.* **2020**, *13*, 849. [CrossRef]
14. Chen, Z.Q.; He, C.; Wu, D.; Xu, G.W.; Yang, W.B. Fracture evolution and energy mechanism of deep-buried carbonaceous slate. *Acta Geotech.* **2017**, *12*, 1243–1260. [CrossRef]
15. Cai, X.; Zhou, Z.L.; Tan, L.H.; Zang, H.Z.; Song, Z.Y. Fracture behavior and damage mechanisms of sandstone subjected to wetting-drying cycles. *Eng. Fract. Mech.* **2020**, *234*, 107109. [CrossRef]

16. Chen, Y.; Cao, P.; Mao, D.W.; Pu, C.Z.; Fan, X. Morphological analysis of sheared rock with water-rock interaction effect. *Int. J. Rock Mech. Min. Sci.* **2014**, *70*, 264–272. [CrossRef]
17. Li, X.Z.; Jia, Y.X.; Zhang, Q.S.; Qi, C.Z. A micro–macro model of pore pressure effect on shear fracture in brittle rocks under compression. *Arch. Appl. Mech.* **2022**, *92*, 1157–1165. [CrossRef]
18. Du, K.; Li, X.F.; Tao, M.; Wang, S.F. Experimental study on acoustic emission (AE) characteristics and crack classiture in several basic lab tests. *Int. J. Rock Mech. Min. Sci.* **2020**, *133*, 104411. [CrossRef]
19. Zhang, J.Z.; Zhou, X.P. AE event rate characteristics of flawed granite: From damage stress to ultimate failure. *Geophys. J. Int.* **2020**, *222*, 795–814. [CrossRef]
20. Zhang, J.Z.; Zhou, X.P. Forecasting catastrophic rupture in brittle rocks using precursory ae time series. *J. Geophys. Res. Sol. Earth* **2020**, *125*, e2019J–e19276J. [CrossRef]
21. Niandou, H.; Shao, J.F.; Henry, J.P.; Fourmaintraux, D. Laboratory investigation of the mechanical behaviour of Tournemire shale. *Int. J. Rock Mech. Min. Sci.* **1997**, *34*, 3–16. [CrossRef]
22. Kuila, U.; Dewhurst, D.N.; Siggins, A.F.; Raven, M.D. Stress anisotropy and velocity anisotropy in low porosity shale. *Tectonophysics* **2011**, *503*, 34–44. [CrossRef]
23. Xu, F.; Yang, C.H.; Guo, Y.T.; Wang, L.; Hou, Z.K.; Li, H.R.; Hu, X.M.; Wang, T.T. Effect of bedding planes on wave velocity and AE characteristics of the Longmaxi shale in China. *Arab. J. Geosci.* **2017**, *10*, 141. [CrossRef]
24. Yang, S.Q.; Yin, P.F.; Li, B.; Yang, D.S. Behavior of transversely isotropic shale observed in triaxial tests and Brazilian disc tests. *Int. J. Rock Mech. Min. Sci.* **2020**, *133*, 104435. [CrossRef]
25. AL-Bazali, T. The impact of water content and ionic diffusion on the uniaxial compressive strength of shale. *Egypt. J. Pet.* **2013**, *22*, 249–260. [CrossRef]
26. Sone, H.; Zoback, M.D. Time-dependent deformation of shale gas reservoir rocks and its long-term effect on the in situ state of stress. *Int. J. Rock Mech. Min. Sci.* **2014**, *69*, 120–132. [CrossRef]
27. Rybacki, E.; Reinicke, A.; Meier, T.; Makasi, M.; Dresen, G. What controls the mechanical properties of shale rocks?—Part I: Strength and Young's modulus. *J. Petrol. Sci. Eng.* **2015**, *135*, 702–722. [CrossRef]
28. Lyu, Q.; Ranjith, P.G.; Long, X.; Kang, Y.; Huang, M. A review of shale swelling by water adsorption. *J. Nat. Gas Sci. Eng.* **2015**, *27*, 1421–1431. [CrossRef]
29. Ban, Y.X.; Xie, Q.; Duan, J.; Fu, X. Influences of inclined pre-existing flaw on shale failure modes in uniaxial compression tests. *Minerals* **2022**, *12*, 1330. [CrossRef]
30. Yang, C.H.; Mao, H.J.; Wang, X.C.; Li, X.H.; Chen, J.W. Study on variation of microstructure and mechanical properties of water-weakening slates. *Chin. Rock Soil Mech.* **2006**, 2090–2098. [CrossRef]
31. Zhu, B.L.; Li, X.N.; Wu, X.Y.; Wang, Y.J. Experimental study of micro-characteristics of swelling for black shale under influence of water. *Chin. J. Rock Mech. Eng.* **2015**, *34*, 3896–3905. [CrossRef]
32. Zhang, J.Z.; Zhou, X.P.; Zhou, L.S.; Berto, F. Progressive failure of brittle rocks with non-isometric flaws: Insights from acousto-optic-mechanical (AOM) data. *Fatigue Fract. Eng. Mater. Struct.* **2019**, *42*, 1787–1802. [CrossRef]
33. Triantis, D.; Kourkoulis, S.K. An alternative approach for representing the data provided by the acoustic emission technique. *Rock Mech. Rock Eng.* **2018**, *51*, 2433–2438. [CrossRef]
34. Lennartz-Sassinek, S.; Main, I.G.; Zaiser, M.; Graham, C.G. Acceleration and localization of subcritical crack growth in a natural composite material. *Phys. Rev. E* **2014**, *90*, 052401. [CrossRef]